Charge doping effect on sliding ferroelectricity by first-principles calculations

Pei Wang, Ting Hu,* and Erjun Kan†

Department of Applied Physics and MIIT Key Laboratory of Semiconductor Microstructure and Quantum Sensing, Nanjing University of Science and Technology, Nanjing, Jiangsu 210094, People's Republic of China

(Received 16 April 2024; revised 17 May 2024; accepted 28 May 2024; published 20 June 2024)

Sliding ferroelectric materials present a promising avenue for achieving out-of-plane ferroelectricity in two-dimensional systems, yet further research is imperative to elucidate their intricate microscopic mechanisms. Here, we investigated the charge doping effect on sliding ferroelectricity by first-principles calculations. We found that the ferroelectric polarization and conductivity can coexist at low doping concentrations. The ferroelectric polarization decreases with increasing doping concentration when introducing electrons/holes into the bilayer sliding ferroelectricity with semiconducting character. The rate of decrease is determined by the occupancy ratio of each layer in the conduction and valence bands.

DOI: 10.1103/PhysRevB.109.235426

I. INTRODUCTION

Ferroelectric materials with switchable spontaneous electrical polarization under the Curie temperature hold significant promise for nonvolatile memory devices with advantages such as fast read/write speed, high-density storage, and low power consumption [1–5]. However, the rapidly growing demand for miniaturized devices poses significant challenges for conventional bulk ferroelectric materials like $BaTiO_3$ and $PbTiO_3$. As their thickness decreases to a certain size, the ferroelectric polarization will be difficult to remain stable due to the finite-size effect and depolarizing electrostatic field, which poses a significant bottleneck in the application of ferroelectric nanodevices [6,7].

In recent years, scientists have conducted a significant number of research on two-dimensional (2D) van der Waals ferroelectric materials, among which compounds from groups IV-VI [8,9], CIPS [10,11], In_2Se_3 [12,13] and $d1T$-$MoTe_2$ [14] exhibit intrinsic ferroelectric properties. However, such materials remain relatively scarce due to limitations imposed by lattice symmetry. In 2017, Wu *et al.* proposed the concept of sliding ferroelectricity, which is designed by artificially stacking nonpolar two-dimensional materials [15]. Stacking breaks the symmetry of the original monolayer structure, leading to out-of-plane ferroelectric polarization, and the two polarization states can be switched through in-plane interlayer shear motion without any necessary atomic displacements in out-of-plane directions [5,16,17]. This greatly expands the candidate materials for two-dimensional ferroelectrics. Verification has been achieved in sliding ferroelectric materials such as BN [15,18–22], MX_2 (M = Mo and W, X = S and Se) [15,23–26], $1T'$-WTe_2 [27–30], ReS_2 [31], and multilayer graphene [32–34].

Although sliding ferroelectricity has brought some new perspectives for low-dimensional ferroelectricity, further in-depth research is imperative to comprehensively elucidate its underlying microscopic mechanisms. What are the key factors that influence the strength of ferroelectric polarization? How does interfacial ferroelectricity coexist harmoniously with in-plane conductivity? Especially, how does electrostatic doping affect ferroelectricity when ferroelectric materials are incorporated into devices? In this work, we investigated the charge doping effect on sliding ferroelectricity through first-principles calculations. We found that the ferroelectric polarization decreases with increasing doping concentration when introducing electrons/holes into the bilayer sliding ferroelectricity. The rate of decrease is related to the occupancy ratio of each layer in the conduction and valence bands. The greater the difference in the proportion occupied by each layer, the faster the rate of decrease.

II. COMPUTATIONAL DETAILS

In this work, our all first-principles calculations based on the density functional theory (DFT) were performed using the Vienna *Ab Initio* Simulation Package (VASP) [35,36] within the projected augmented wave (PAW) potentials [37] with the generalized gradient approximation in the Perdew-Burke-Ernzerhof (PBE) [38] to describe the exchange-correlation potential. To accurately describe the interlayer van der Waals interactions, we adopted the semiempirical correction method presented by Grimme (DFT-D3) [39]. The plane-wave cutoff energy for the wave function was set to be 500 eV, and a large vacuum space was set in the vertical direction so the nearest distance between two neighboring bilayer was greater than 15 Å to diminish interaction between adjacent slabs. A Γ-centered $9 \times 9 \times 1$ Monkhorst-Pack [40] k-mesh was used for Brillion zone sampling. Electronic minimization was performed with an energy tolerance of 10^{-5} eV, and ionic relaxation was performed with a force tolerance of 0.005 eV/Å on each ion. Spin-orbit interactions were

*Contact author: thu@njust.edu.cn
†Contact author: ekan@njust.edu.cn

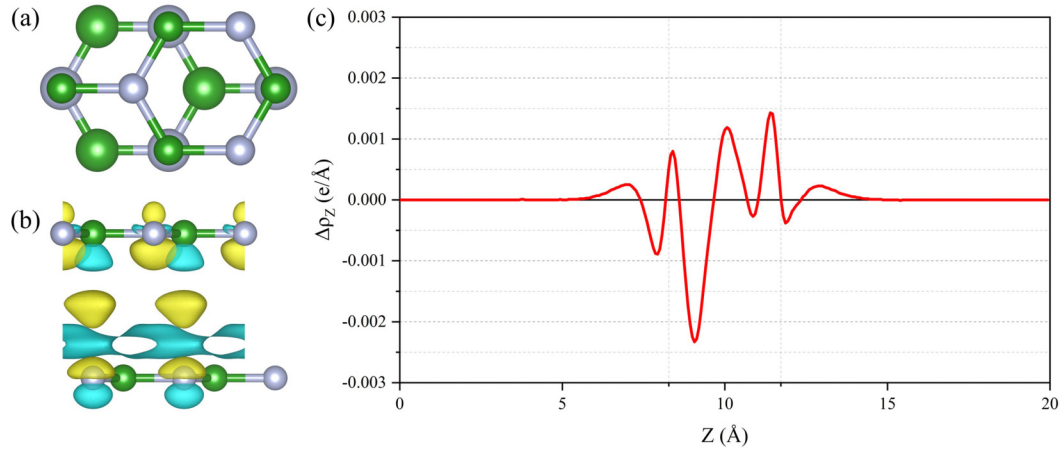

FIG. 1. Polarization in *AB* stacked bilayer BN. (a) Top view illustration of the atomic arrangement for bilayer BN. To distinguish between the top and bottom layers, the atoms in the bottom layer are represented by larger radius. Nitrogen and boron atoms are shown in silver and green, respectively. (b) The side view of the differential charge density diagram. The yellow and cyan areas indicate the regions that gained and lost electrons, respectively. (c) The plane-averaged difference charge density in the z-axis direction. The two vertical lines in the diagram show where the two individual monolayers are located.

included in the calculation of transition metals. The Berry phase theory [41] was employed to evaluate the values of vertical polarization. The transition states of reactions were determined by the climbing image nudged elastic band (CI-NEB) method [42].

III. RESULTS AND DISCUSSION

Hexagonal boron nitride (BN) is a layered compound with a honeycomb lattice structure. Single-layer boron nitride can be obtained from bulk boron nitride crystals using mechanical exfoliation techniques, similar to graphene [43]. Figure 1(a) shows the structure of *AB* stacked bilayer *h*-BN. It is observed that the N atoms in the bottom layer are directly above the B atoms in the top layer, while the B atoms in the bottom layer sit at the center of the hexagon and do not align vertically with the N atoms in the top layer. This stacking order breaks the inversion symmetry and M_Z symmetry, endowing it with out-of-plane ferroelectricity. We calculated its ferroelectric polarization $P_Z = 0.597$ pC/m using the Berry phase method. To further elucidate the origin of out-of-plane polarization, we calculated the differential charge density between the bilayer BN and two isolated monolayers. As shown in Fig. 1(b), we observe the accumulation and depletion of charges between two monolayers. The inequivalence between the two layers results in a net charge transfer, leading to out-of-plane vertical polarization. This can be visualized by the differential charge densities $\Delta\rho(z) = \rho_{\mathrm{BN}}(z) - \rho_{\mathrm{top}}(z) - \rho_{\mathrm{bottom}}(z)$, where $\rho_{\mathrm{BN}}(z)$, $\rho_{\mathrm{top}}(z)$, and $\rho_{\mathrm{bottom}}(z)$ are the plane-averaged charge densities of the bilayer BN and the isolated top and bottom layers [44]. We can see in Fig. 1(c) that charges near the top layer accumulate while charges near the bottom layer deplete, indicating that charges mainly transfer from the bottom layer to the top layer, resulting in out-of-plane polarization.

Next, we performed doping calculations on the bilayer sliding ferroelectric material BN to explore the influence of electrostatic doping on ferroelectric polarization. Since the doped system is not electrically neutral, we cannot directly use the Berry phase method to calculate the ferroelectric polarization. The bilayer structure lacks inversion symmetry, allowing for net charge transfer between the top and bottom layers, further generating interface dipoles accompanied by the formation of an electrostatic potential difference $\Delta\Phi$ at the interface. Therefore, we can reflect the changes in polarization by calculating the interlayer charge difference $\Delta\rho$ and $\Delta\Phi$ of the bilayer structure under different doping concentrations in Figs. 2(e) and 2(f). For the system of polarization pointing downwards, we define the interlayer charge difference as $\Delta\rho(e) = \rho_{\mathrm{top}} - \rho_{\mathrm{bottom}}$, where ρ_{top} and ρ_{bottom} are the charges of the top and bottom layers of the bilayer BN, respectively. ρ_{top} can be obtained by integrating plane-averaged differential charge density from the center of the bilayer BN to the top in Figs. 2(c) and 2(d): $\rho_{\mathrm{top}} = \int_{Z/2}^{Z} \Delta\rho(z)dz$. ρ_{bottom} can be obtained by integrating from the center of the bilayer BN to the bottom: $\rho_{\mathrm{bottom}} = \int_{0}^{Z/2} \Delta\rho(z)dz$. To present a more intuitive visualization of the reduction in polarization intensity, we adopt the initial structure as a benchmark, highlighting the percentage changes in polarization intensity across various charge doping concentrations. We find that both the $\Delta\rho$ and $\Delta\Phi$ exhibit a decreasing trend with an increase in doping concentration, indicating that the polarization decreases with increasing doping concentration. In order to explain the reason for the suppression of the polarization, we analyze the differential charge density diagram and planar-average charge density difference at different doping concentrations. As shown in Figs. 2(a)–2(d), we find that when electrons/holes are introduced into the system, more electrons populate the bottom layer compared to the top layer, while more holes occupy the top layer. Therefore, for bilayer BN, electrostatic doping decreases the charge difference between the layers, leading to a decrease in net polarization.

The above analysis indicates that electrostatic doping has a suppressive effect on the ferroelectricity of the bilayer BN. However, the mechanism behind the trend of ferroelectric polarization changing with doping concentration is not yet

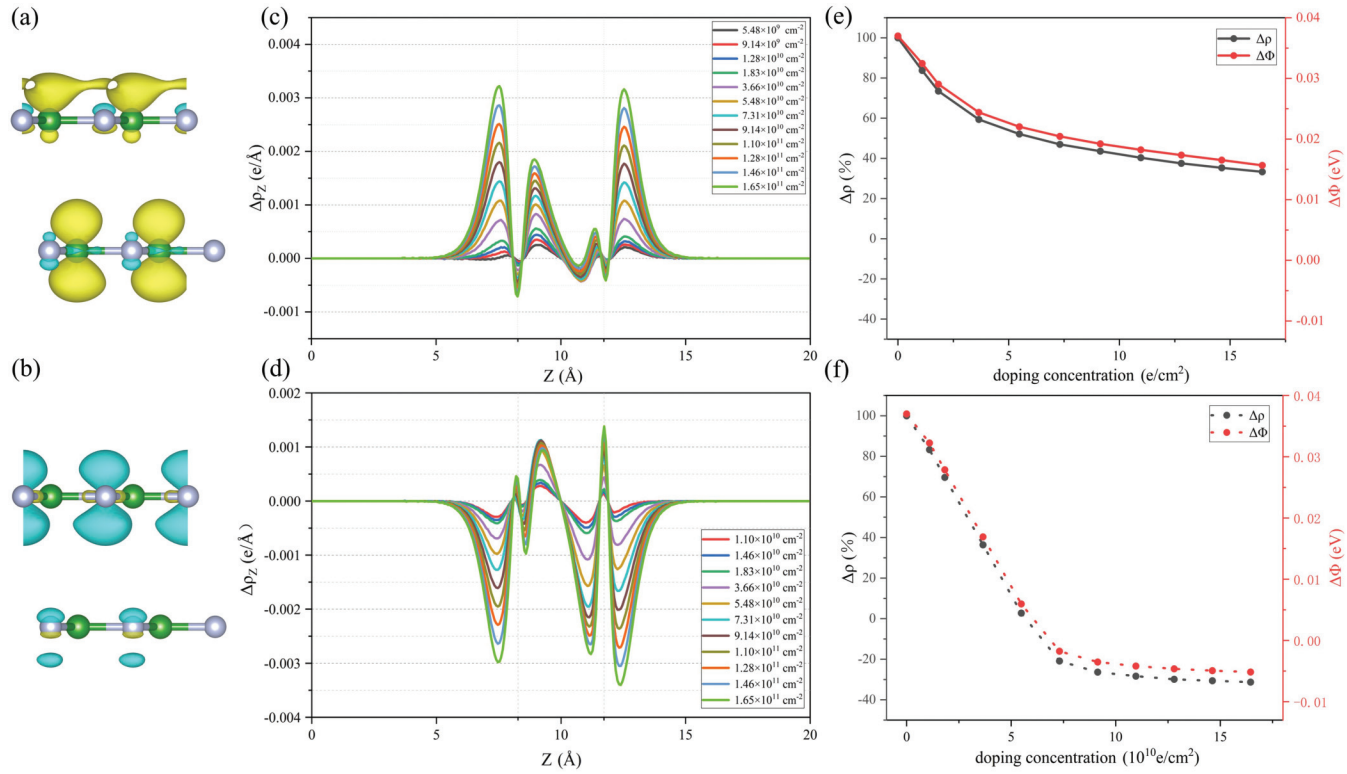

FIG. 2. Electrostatic doping in bilayer BN. The differential charge density diagram of (a) electron and (b) hole doping obtained by subtracting the charge density of the undoped system from that of the doped system. The plane-averaged differential charge density profile at difference (c) electrons and (d) holes doping concentrations in the z-axis direction; the doping concentrations are written in the labeling and different doping concentrations are indicated by different color lines. $\Delta\rho(z) = \rho_{\text{doped}}(z) - \rho_{\text{undoped}}(z)$, where $\rho_{\text{doped}}(z)$ and $\rho_{\text{undoped}}(z)$ are the planar average charge density for doped and undoped systems. The extent of the decrease in the top and bottom layer charge difference (black) and electrostatic potential difference (red) with (e) electron and (f) hole doping concentration.

clear and requires further elucidation. Therefore, we analyzed the band structure of bilayer BN and the projected band structures at the top and bottom layer in Figs. 3(a)–3(c). We observe that the band splits due to the built-in electric field affecting the energies of the top and bottom electrons. Comparing Figs. 3(b) and 3(c), we find states from both layers in conduction and valence bands, but the occupancy ratio of each layer is different. The blue lines are darker at the conduction-band minimum (CBM) and the red is darker at the valence-band maximum (VBM). This indicates that the CBM is mainly contributed by electrons in the bottom layer, whereas the VBM is mainly contributed by electrons in the

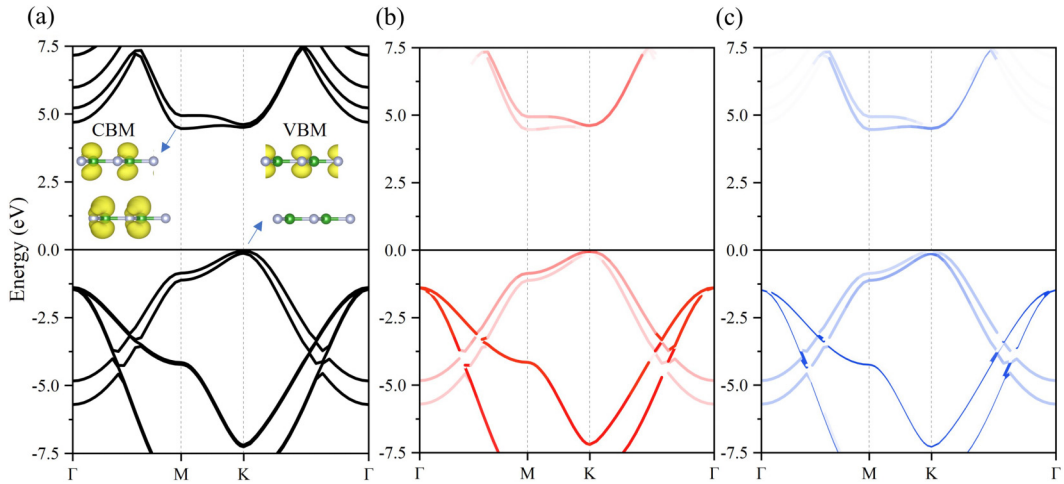

FIG. 3. Band structures in bilayer BN. The band structures of (a) *AB*-stacked bilayer BN. The illustrations on the left and right sides of the diagram are the partial charge density in the CBM and VBM, respectively. The projected band structures of (b) top and (c) bottom layer. Shades of color indicate the strength of the contribution of the top (red)/bottom (blue) layer.

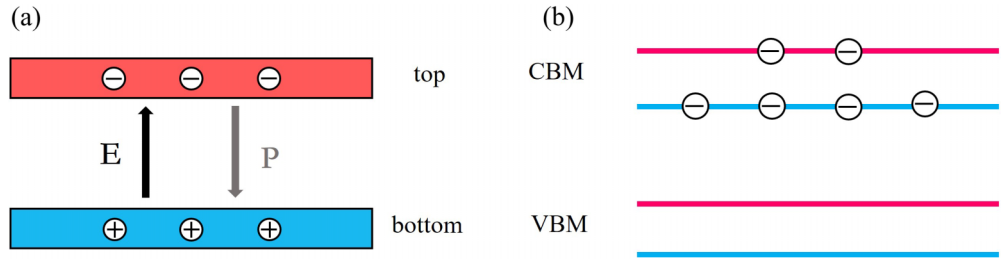

FIG. 4. (a) Bilayer sliding ferroelectric structure model with the red rectangles representing the top layer and the blue rectangles representing the bottom layer. The bilayer structure possesses an upward builtin electric field. (b) Band model near the Fermi level in the bilayer structure. The red and blue colors represent the bands of the top and bottom layers, respectively. The electron model represents the electron filling situation in the top and bottom layers when doping electrons.

top layer. Therefore, during electrostatic doping, the bottom layer is predominantly populated with electrons, while the top layer is primarily occupied by holes.

Additionally, there is a significant difference in the color intensity of the lines in the VBM, indicating a larger contribution difference between the bilayers. The insets in Fig. 3(a) show the partial charge density at the CBM and VBM. The insets and the contributions of each layer atom at CBM and VBM (see Supplemental Material Table S1 [45]) reveal that the CBM is primarily contributed by the p_z orbitals of B atoms, with a slightly larger contribution from the bottom layer, while the VBM is mainly contributed by p_z orbitals of N atoms in the top layer. So the magnitude of this imbalance is larger for valence band states. Owing to the larger imbalance, the response of bilayer BN to hole doping is more pronounced at the beginning of doping into the system. Simultaneously, we also calculated the partial charge density within the energy range of Fermi level shifts for different doping concentrations, and obtained the degree of imbalance of the occupation of each layer in the conduction (black) and valence (red) bands to determine the trend of ferroelectric polarization with doping concentration. We found that the trend of the imbalance of the occupation of each layer in Fig. S1(a) of the Supplemental Material [45] is consistent with the trend of the influence of doping concentration on the polarization strength in Figs. 2(e) and 2(f). Therefore, the rate of suppression of ferroelectric polarization by doping is related to the occupancy ratio of each layer in the conduction and valence bands. At higher hole doping concentrations in Fig. 2(f), the polarization intensity continuously decreases and even changes direction. We analyzed the projected band structures of the higher doping concentration system and found the occupancy ratio of the top and bottom layers at the VBM changes (see Supplemental Material Fig. S2 [45]). The contribution of the bottom layer becomes greater than that of the top layer, leading to a change in the direction of polarization.

Based on the above analysis, we proposed the following model to describe the effect of electrostatic doping on the bilayer ferroelectric material. As shown in Fig. 4(a), an upward built-in electric field is generated in the bilayer polar material with downward polarization due to the interlayer charge transfer, causing an increase in the potential energy of the electrons in the top layer and a decrease in the potential energy of the electrons in the bottom layer, leading to band splitting. As depicted in Fig. 4(b), the energy bands of the electrons in the top layer (red) correspond to relatively high energies, and the energy bands in the bottom layer (blue) correspond to relatively low energies. If electrons are doped into this system, they will preferentially populate the bottom layer, while hole doping will preferentially occupy the top layer. Therefore, there are relatively more electrons/holes filled in the bottom/top layer at low doping concentrations, reducing the charge difference between the bilayers and suppressing net spontaneous polarization. The different responses to electron and hole doping are determined by the occupation ratio of each layer in the conduction and valence bands. The greater the difference in the occupancy ratio of bilayers, the more pronounced the suppression of polarization.

In order to validate the accuracy of the above model, we further performed calculations on the bilayer sliding ferroelectric MoS_2, $MoSe_2$, $MoTe_2$, WS_2, WSe_2, and WTe_2 systems. Initially, we computed the band and projected band structures of the polar states of them (see Supplemental Material Fig. S4). It was observed that these structures exhibit band splitting phenomena at both the CBM and VBM. Additionally, there is a more prominent contribution from the bottom layer at the CBM and a clearer contribution from the top layer at the VBM. Based on this observation, we hypothesized that adding electrons to the conduction band would fill predominantly in the bottom layer, while adding holes to the valence band would fill predominantly in the top layer. Therefore, doping reduces the interlayer charge difference and suppresses the net polarization. However, the magnitude of the occupancy of the two layers is different in different structures. Combining Fig. S4 and contributions of each layer and atom at the CBM and VBM (see Supplemental Material Table S2), we can conclude that the difference of occupancy ratio between the two layers in the CBM is greater in the structures of MoS_2, $MoSe_2$, $MoTe_2$, and WS_2, while the difference in the VBM is greater in the structures of WSe_2 and WTe_2. As a result, adding electrons to the system has a faster inhibitory effect on the polarization intensity in the first four structures. The net polarization response to hole doping is more pronounced in the latter two structures.

Next, we specifically calculated the effect of $\Delta\rho$ on the MX_2 structures with different doping concentrations to reflect the variation of the polarization. We can clearly see the inhibitory effect of electrostatic doping on the polarization of bilayer ferroelectric materials described above in Fig. S5. Moreover, the extent of response to electrons and holes corresponds to the analysis above, consistent with the difference of occupancy ratio between the two layers in conduction and

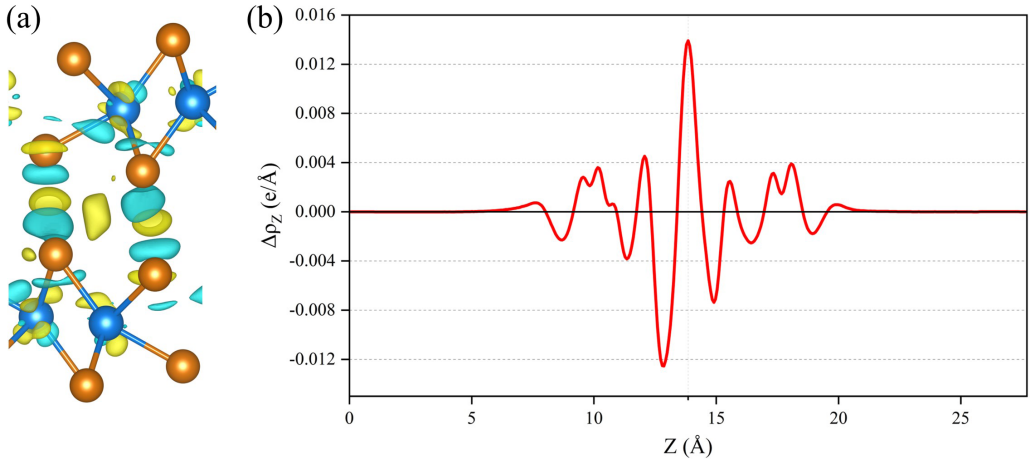

FIG. 5. Polarization in bilayer $1T'$-WTe_2. (a) The side view of the differential charge density. The blue and orange spheres represent W and Te atoms, respectively. The yellow and cyan areas indicate the regions that gained and lost electrons, respectively. (b) The plane-averaged differential charge density between bilayer WTe_2 and two independent monolayers. $\Delta\rho(z) = \rho_{WTe_2}(z) - \rho_{top}(z) - \rho_{bottom}(z)$, where $\rho_{WTe_2}(z)$, $\rho_{top}(z)$, and $\rho_{bottom}(z)$ are the charge densities of the bilayer WTe_2.

valance bands. This can be further validated by comparing Fig. S1(b) with Fig. S5(a).

We found that the model proposed is generally applicable to the semiconductor properties of the bilayer sliding ferroelectric material. Naturally, the question arises of whether this model can be extended to bilayer ferroelectric material with metallic properties. To address this inquiry, we investigated the doping effect on bilayer $1T'$-WTe_2, which is experimentally validated metallic ferroelectricity. First, we calculated the differential charge density and planar average charge density of the bilayer WTe_2, demonstrating that the interlayer charge distribution is uneven in Figs. 5(a) and 5(b). Subsequently, we calculated its band and projected band in Fig. 6, finding that the band structure still exhibits layered characteristics. We speculate that the effect of doping on ferroelectric polarization is also related to the occupancy ratio of each layer near the Fermi level. However, the band structure near the Fermi level is quite complex, and the situation of each layer cannot be determined as easily as analyzing the semiconductor system, so further calculations are needed to verify this.

Next, we calculated the differential charge density and planar-average differential charge density under different doping concentrations and found that electrons still predominantly occupy the bottom layer in Figs. 7(a) and 7(c), while more holes are populated in the top layer in Figs. 7(b) and 7(d), indicating that doping still has an inhibitory effect on ferroelectric polarization. We calculated $\Delta\rho$ and $\Delta\Phi$ to reflect the variation of ferroelectric polarization with doping concentration in Figs. 7(e) and 7(f). We found that the polarization decreases as the doping concentration increases. As shown in Fig. S6, we find that in the calculated energy range, the contribution from the bottom layer is still more prominent above the Fermi level, while the contribution from the top layer is still slightly higher below the Fermi level, and the difference of occupancy ratio between the two layers is larger for conduction band states. The difference follows the same trend as the variation of polarization intensity with doping

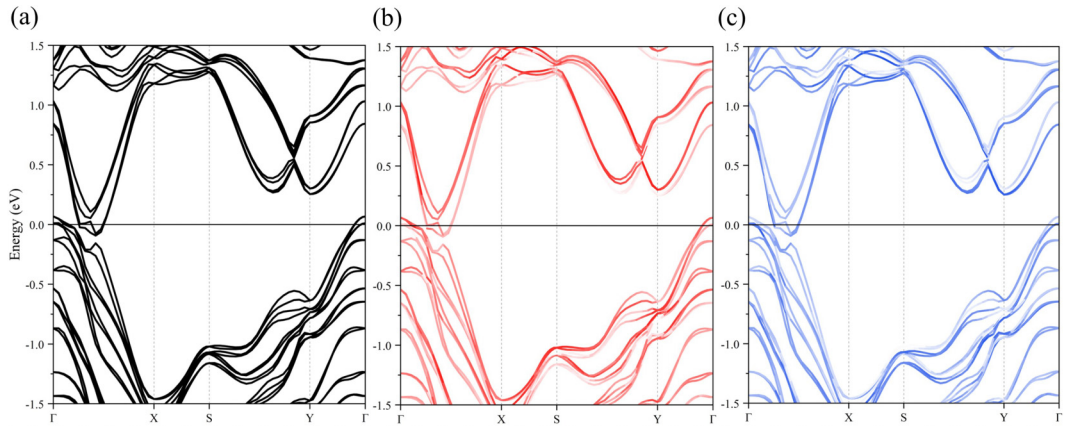

FIG. 6. Band structures of bilayer $1T'$-WTe_2. (a)–(c) The total band structure, the projected band structure on the top layer, and the projected band structure on the bottom layer, respectively. In the projected band structures, the shading of colors indicates the strength of the contribution of electrons from the top (red)/bottom (blue) layer.

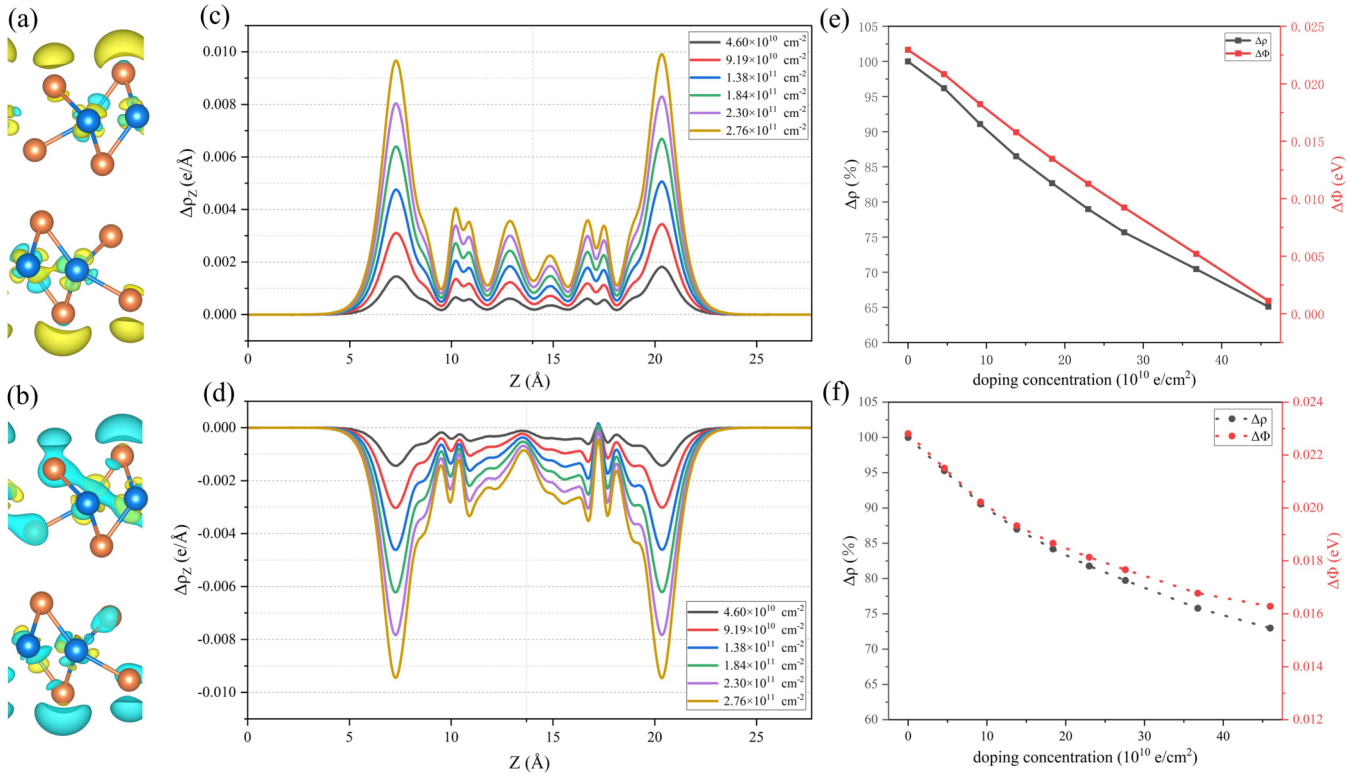

FIG. 7. Electrostatic doping of bilayer 1T'-WTe_2. The differential charge density diagram of (a) electron and (b) hole doping obtained by subtracting the charge density of the undoped system from that of the doped system. The plane-averaged differential charge density profile at difference (c) electron and (d) hole doping concentrations in the z-axis direction; the doping concentrations are written in the labeling and different doping concentrations are indicated by different color lines. $\Delta\rho = \rho_{\text{doped}}(z) - \rho_{\text{undoped}}(z)$, where $\rho_{\text{doped}}(z)$ and $\rho_{\text{undoped}}(z)$ are the planar average charge density for doped and undoped systems. The extent of the decrease in the top and bottom layer charge difference (black) and electrostatic potential difference (red) with (e) electron and (f) hole doping concentration.

concentration in Figs. 7(e) and 7(f). This indicates that in the metallic WTe_2 system, electrostatic doping continues to inhibit the polarization. However, it cannot be simply concluded that this holds true for other metallic systems, and specific analysis is required for each individual system.

IV. CONCLUSIONS

In conclusion, we have investigated the charge doping effect on ferroelectricity of bilayer sliding ferroelectric systems with semiconducting or metallic properties by first-principles calculations. We found that the polarization strength of sliding ferroelectrics with semiconducting properties decreases with increasing doping concentration and responds differently to electron and hole doping. This is because the intrinsic built-in electric field causes band splitting, resulting in different occupancy ratio in the conduction and valence bands. The greater the magnitude of imbalance occupied by the layers for the conduction (valence) band states, the stronger the inhibitory effect of electron (hole) doping on ferroelectric polarization. However, the band structure near the Fermi level is relatively complex for bilayer sliding ferroelectric materials with metallic properties, requiring a specific analysis for each case. Charge doping remains inhibitory to its ferroelectric polarization for bilayer T'-WTe_2 and the degree of suppression is related to the occupancy ratio of each layer near the Fermi level. This conclusion may be extrapolated to additional bilayer sliding ferroelectric materials, facilitating an in-depth analysis of the impact of electrostatic doping on ferroelectric polarization. Such an investigation is instrumental in unraveling the nature of polarization within bilayer sliding ferroelectrics, thereby propelling forward the sophisticated design and pragmatic application of low-dimensional nanoferroelectric materials.

ACKNOWLEDGMENTS

The work was supported by the NSFC (Grants No. 51872142, No. 11774173, No. 51790492, and No. 51522206), the NSF of Jiangsu Province (Grant No. BK20170831), and the Fundamental Research Funds for the Central Universities (Grants No. 30920021148, No. 30915011203, and No. 30918011334). We also acknowledge the support from the Tianjing Supercomputer Centre, Shanghai Supercomputer Center, and High-Performance Computing Center of Collaborative Innovation Center of Advanced Microstructures.

[1] V. Garcia and M. Bibes, Ferroelectric tunnel junctions for information storage and processing, Nat. Commun. **5**, 4289 (2014).

[2] J. Y. Kim, M.-J. Choi, and H. W. Jang, Ferroelectric field effect transistors: Progress and perspective, APL Mater. **9**, 021102 (2021).

[3] W. Gao, Y. Zhu, Y. Wang, G. Yuan, and J.-M. Liu, A review of flexible perovskite oxide ferroelectric films and their application, J. Mater. **6**, 1 (2020).

[4] X. Wang, P. Yu, Z. Lei, C. Zhu, X. Cao, F. Liu, L. You, Q. Zeng, Y. Deng, C. Zhu, J. Zhou, Q. Fu, J. Wang, Y. Huang, and Z. Liu, Van der Waals negative capacitance transistors, Nat. Commun. **10**, 3037 (2019).

[5] M. H. Wu, Two-Dimensional van der Waals Ferroelectrics: Scientific and technological opportunities, ACS Nano **15**, 9229 (2021).

[6] C. Duan, R. F. Sabirianov, W. Mei, S. S. Jaswal, and E. Y. Tsymbal, Interface effect on ferroelectricity at the nanoscale, Nano Lett. **6**, 483 (2006).

[7] J. Junquera and P. Ghosez, Critical thickness for ferroelectricity in perovskite ultrathin films, Nature (London) **422**, 506 (2003).

[8] K. Chang, J. Liu, H. Lin, N. Wang, K. Zhao, A. Zhang, F. Jin, Y. Zhong, X. Hu, W. Duan, Q. Zhang, L. Fu, Q.-K. Xue, X. Chen, and S.-H. Ji, Discovery of robust in-plane ferroelectricity in atomic-thick SnTe, Science **353**, 274 (2016).

[9] M. Wu and X. Zeng, Intrinsic ferroelasticity and/or multiferroicity in two-dimensional phosphorene and phosphorene analogues, Nano Lett. **16**, 3236 (2016).

[10] F. Liu, L. You, K. L. Seyler, X. Li, P. Yu, J. Lin, X. Wang, J. Zhou, H. Wang, H. He, S. T. Pantelides, W. Zhou, P. Sharma, X. Xu, P. M. Ajayan, J. Wang, and Z. Liu, Room-temperature ferroelectricity in $CuInP_2S_6$ ultrathin flakes, Nat. Commun. **7**, 12357 (2016).

[11] J. Zheng, Y. Zhao, H. Hu, Y. Shen, Y. Tan, W. Tong, P. Xiang, N. Zhong, F. Yue, and C. Duan, Ferroelectric control of pseudospin texture in $CuInP_2S_6$ monolayer, J. Phys.: Condens. Matter **34**, 204001 (2022).

[12] W. Ding, J. Zhu, Z. Wang, Y. Gao, D. Xiao, Y. Gu, Z. Zhang, and W. Zhu, Prediction of intrinsic two-dimensional ferroelectrics in In_2Se_3 and other III_2-VI_3 van der Waals materials, Nat. Commun. **8**, 14956 (2017).

[13] J. Xiao, H. Zhu, Y. Wang, W. Feng, Y. Hu, A. Dasgupta, Y. Han, Y. Wang, D. A. Muller, L. W. Martin, P. Hu, and X. Zhang, Intrinsic two-dimensional ferroelectricity with dipole locking, Phys. Rev. Lett. **120**, 227601 (2018).

[14] S. Yuan, X. Luo, H. Chan, C. Xiao, Y. Dai, M. Xie, and J. Hao, Room-temperature ferroelectricity in $MoTe_2$ down to the atomic monolayer limit, Nat. Commun. **10**, 1775 (2019).

[15] L. Li and M. Wu, Binary compound bilayer and multilayer with vertical polarizations: Two-dimensional ferroelectrics, multiferroics, and nanogenerators, ACS Nano **11**, 6382 (2017).

[16] E. Y. Tsymbal, Two-dimensional ferroelectricity by design, Science **372**, 1389 (2021).

[17] Z. Wang, Z. Gui, and L. Huang, Sliding ferroelectricity in bilayer honeycomb structures: A first-principles study, Phys. Rev. B **107**, 035426 (2023).

[18] Y. Liang, S. Shen, B. Huang, Y. Dai, and Y. Ma, Intercorrelated ferroelectrics in 2D van der Waals materials, Mater. Horiz. **8**, 1683 (2021).

[19] W. Jiang, C. Liu, X. Ma, X. Yu, S. Hu, X. Li, L. A. Burton, Y. Liu, Y. Chen, P. Guo, X. Kong, L. Bellaiche, and W. Ren, Anomalous ferroelectricity and double-negative effects in bilayer hexagonal boron nitride, Phys. Rev. B **106**, 054104 (2022).

[20] K. Yasuda, X. Wang, K. Watanabe, T. Taniguchi, and P. Jarillo-Herrero, Stacking-engineered ferroelectricity in bilayer boron nitride, Science **372**, 1458 (2021).

[21] S. L. Moore, C. J. Ciccarino, D. Halbertal, L. J. McGilly, N. R. Finney, K. Yao, Y. Shao, G. Ni, A. Sternbach, E. J. Telford, B. S. Kim, S. E. Rossi, K. Watanabe, T. Taniguchi, A. N. Pasupathy, C. R. Dean, J. Hone, P. J. Schuck, P. Narang, and D. N. Basov, Nanoscale lattice dynamics in hexagonal boron nitride moire superlattices, Nat. Commun. **12**, 5741 (2021).

[22] M. V. Stern, Y. Waschitz, W. Cao, I. Nevo, K. Watanabe, T. Taniguchi, E. Sela, M. Urbakh, O. Hod, and M. B. Shalom, Interfacial ferroelectricity by van der Waals sliding, Science **372**, 1462 (2021).

[23] Xirui. Wang, K. Yasuda, Y. Zhang, S. Liu, K. Watanabe, T. Taniguchi, J. Hone, L. Fu, and P. Jarillo-Herrero, Interfacial ferroelectricity in rhombohedral-stacked bilayer transition metal dichalcogenides, Nat. Nanotechnol. **17**, 367 (2022).

[24] A. Weston, E. G. Castanon, V. Enaldiev, F. Ferreira, S. Bhattacharjee, S. Xu, H. Corte-León, Z. Wu, N. Clark, A. Summerfield, T. Hashimoto, Y. Gao, W. Wang, M. Hamer, H. Read, L. Fumagalli, A. V. Kretinin, S. J. Haigh, O. Kazakova, A. K. Geim *et al.*, Interfacial ferroelectricity in marginally twisted 2D semiconductors, Nat. Nanotechnol. **17**, 390 (2022).

[25] P. Meng, Y. Wu, R. Bian, E. Pan, B. Dong, X. Zhao, J. Chen, L. Wu, Y. Sun, Q. Fu, Q. Liu, D. Shi, Q. Zhang, Y. W. Zhang, Z. Liu, and F. Liu, Sliding induced multiple polarization states in two-dimensional ferroelectrics, Nat. Commun. **13**, 7696 (2022).

[26] Z. Lin, C. Si, S. Duan, C. Wang, and W. Duan, Rashba splitting in bilayer transition metal dichalcogenides controlled by electronic ferroelectricity, Phys. Rev. B **100**, 155408 (2019).

[27] Q. Yang, C. Song, and S. Meng, Laser-induced enhancement of vertical polarization in ferroelectric bilayer WTe_2, J. Phys.: Condens. Matter **34**, 424003 (2022).

[28] Q. Yang, M. Wu, and J. Li, Origin of two-dimensional vertical ferroelectricity in WTe_2 bilayer and multilayer, J. Phys. Chem. Lett. **9**, 7160 (2018).

[29] X. Liu, Y. Yang, T. Hu, G. Zhao, C. Chen, and W. Ren, Vertical ferroelectric switching by in-plane sliding of two-dimensional bilayer WTe_2, Nanoscale **11**, 18575 (2019).

[30] S. C. de la Barrera, Q. R. Cao, Y. Gao, Y. Gao, V. S. Bheemarasetty, J. Q. Yan, D. G. Mandrus, W. G. Zhu, D. Xiao, and B. M. Hunt, Direct measurement of ferroelectric polarization in a tunable semimetal, Nat. Commun. **12**, 5298 (2021).

[31] Y. Wan, T. Hu, X. Mao, J. Fu, K. Yuan, Y. Song, X. Gan, X. Xu, M. Xue, X. Cheng, C. Huang, J. Yang, L. Dai, H. Zeng, and E. Kan, Room-temperature ferroelectricity in 1T'-ReS_2 multilayers, Phys. Rev. Lett. **128**, 067601 (2022).

[32] A. Garcia-Ruiz, V. Enaldiev, and A. McEllistrim, V. I. Fal'ko, Mixed-stacking few-layer graphene as an elemental weak ferroelectric material, Nano Lett. **23**, 4120 (2023).

[33] L. Yang, S. Ding, J. Gao, and M. Wu, Atypical sliding and moire ferroelectricity in pure multilayer graphene, Phys. Rev. Lett. **131**, 096801 (2023).

[34] S. S. Atri, W. Cao, B. Alon, N. Roy, M. V. Stern, V. Falko, M. Goldstein, L. Kronik, M. Urbakh, O. Hod, and M. Ben Shalom, Spontaneous electric polarization in graphene polytypes, Adv. Phys. Res. **3**, 2300095 (2024).

[35] G. Kresse and J. Furthmller, Efficient iterative schemes for *ab initio* total-energy calculations using a plane-wave basis set, Phys. Rev. B **54**, 11169 (1996).

[36] G. Kresse and J. Furthmüller, Efficiency of ab-initio total energy calculations for metals and semiconductors using a plane-wave basis set, Comput. Mater. Sci. **6**, 15 (1996).

[37] G. Kresse and D. Joubert, From ultrasoft pseudopotentials to the projector augmented-wave method, Phys. Rev. B **59**, 1758 (1999).

[38] J. P. Perdew, K. Burke, and M. Ernzerhof, Generalized gradient approximation made simple, Phys. Rev. Lett. **77**, 3865 (1996).

[39] S. Grimme, J. Antony, S. Ehrlich, and H. Krieg, A consistent and accurate *ab initio* parametrization of density functional dispersion correction (DFT-D) for the 94 elements H-Pu, J. Phys. Chem. Lett. **132**, 154104 (2010).

[40] M. Methfessel and A. T. Paxton, High-precision sampling for Brillouin-zone integration in metals, Phys. Rev. B **40**, 3616 (1989).

[41] R. D. King-Smith and D. Vanderbilt, Theory of polarization of crystalline solids, Phys. Rev. B **47**, 1651 (1993).

[42] G. Henkelman, B. P. Uberuaga, and H. Jónsson, A climbing image nudged elastic band method for finding saddle points and minimum energy paths, J. Chem. Phys. **113**, 9901 (2000).

[43] R. V. Gorbachev, I. Riaz, R. R. Nair, R. Jalil, L. Britnell, B. D. Belle, E. W. Hill, K. S. Novoselov, K. Watanabe, T. Taniguchi, A. K. Geim, and P. Blake, Hunting for monolayer boron nitride: Optical and Raman signatures, Small **7**, 465 (2011).

[44] N. X. Vei Wang, J.-C. Liu, G. Tang, and W.-T. Geng, VASPKIT: A user-friendly interface facilitating high-throughput computing and analysis using VASP code, Comput. Phys. Commun. **267**, 108033 (2021).

[45] See Supplemental Material at http://link.aps.org/supplemental/10.1103/PhysRevB.109.235426 for the degrees of imbalance in the conduction band (CB) state and valence band (VB) state of bilayer *h*-BN, MX_2 and $1T'$-WTe_2, and the band structures of MX_2 and the doping effect on their ferroelectric polarization.